Thermal behaviour analysis of lithium-ion battery at elevated temperature using deconvolution method

CrossMark

Ping Ping [a], Qingsong Wang [a,*], Peifeng Huang [a], Jinhua Sun [a,*], Chunhua Chen [b]

[a] State Key Laboratory of Fire Science, University of Science and Technology of China, Hefei 230026, PR China
[b] Department of Materials Science & Engineering, University of Science and Technology of China, Hefei 230026, PR China

HIGHLIGHTS

- We propose a deconvolution method to study thermal behaviour of cells.
- Thermal runaway reactions of Li_xCoO_2/Li_xC_6 system are identified in detail.
- A short circuit reaction occurring after the melting of separator is found.
- The short circuit generates heat and reduces thermal stability of the full cell.
- Heat of reactions related to Li_xCoO_2 dominate the heat generation of a full cell.

ARTICLE INFO

ABSTRACT

The fire and explosion potential risk of Li-ion battery is mainly caused by thermal runaway reactions. A deconvolution method has been proposed to analyze the complex thermal reactions obtained from a reaction, isothermal and scanning calorimeter (C80 microcalorimeter) in this paper. Thermal behaviours of both single electrode system and full cell system under elevated temperature are clearly identified, and separate kinetics is calculated based on the deconvoluted data. According to the analysis, thermal runaway reactions of Li_xCoO_2/Li_xC_6 full cell system are comprised by the solid electrolyte interface (SEI) breakdown, melting of separator, short circuit of positive–negative materials, Li_xCoO_2 disproportionation, lithium (in Li_xC_6)-electrolyte reaction, further decomposition of Li_xCoO_2, oxidation of decomposition products of electrolyte and thermal reactions involving polyvinylidene fluoride (PVDF), etc. The thermal stability of SEI, heat generation of positive material and melting temperature of separator are identified as the critical factors that influence the thermal stability of full cell. It is possible to utilize the method for the thermal analysis and the identification of the key factors to thermal control of Li-ion batteries for energy storage and power supply applications.

© 2014 Elsevier Ltd. All rights reserved.

1. Introduction

Li-ion batteries are currently the predominant power source for hand-held and portable electronic devices, and are being used increasingly in electric vehicles, hybrid electric vehicles and energy storage system [1–3]. However, safety issues are always one of the main reasons delaying broad application of Li-ion batteries in the expanding energy storage markets [4–6]. Thermal and electrical abuses in the battery reactions occur at a high temperature under conditions of heating, crushing, or short-circuit [7–10]. Thermal runaway occurs when an exothermic reaction goes out of control, that is the reaction rate increases due to an increase in temperature causing a further increase in temperature and hence a further increase in the reaction rate [4,11]. These possible reactions occurring inside the battery and the thermal stability of the battery materials have been reported by many researchers using accelerating rate calorimetry (ARC) [12,13], vent sizing package 2 (VSP2) [7,14], differential scanning calorimetry (DSC) [15,16] or C80 microcalorimeter [17,18]. For a single material, its thermal behaviour may be simple and can be easily analyzed. However, for system composed of some coexisting materials, its complex behaviour is difficult to study in detail.

For a real full Li-ion cell, there are at least five kinds of materials in the cell: positive electrode, electrolyte composed of lithium salt and solvents, separator and negative electrode. The polymer separator used in the Li-ion battery melts under elevated

* Corresponding authors. Tel.: +86 551 360 6455; fax: +86 551 360 1669 (Q. Wang). Tel.: +86 551 360 6425; fax: +86 551 360 1669 (J. Sun).
E-mail addresses: pinew@ustc.edu.cn (Q. Wang), sunjh@ustc.edu.cn (J. Sun).

temperature. With the endothermic melting process, the cathode and anode material will contact each other. The possible resulting short in the battery will lead to complex thermal reactions, which would be much different to the reactions occurring in the half cell or simple coexisting system of battery materials. Therefore, it is important to study the thermal behaviour of a real full Li-ion cell. Saito Y studied the heat caused by electrochemical side-reaction of 18,650 batteries during high-rate pulse cycling under 40 °C (isotherm mode) by C80 microcalorimeter [19]. They found that side-reactions affect the surface of the electrodes and enlarge the battery impedance resulting in more heat generation. Hallaj et al. analyzed the thermal behaviour of $LiCoO_2$/graphite (or coke) prismatic and 18,650 batteries when batteries were cycling by ARC-cycler in the temperature range 35–55 °C [20]. For all batteries, the heat effects were found to be exothermic during discharge but endothermic during charge. Ishikawa et al. investigated the thermal properties of $LiCoO_2$/graphite 18,650 batteries at different state of charges using ARC from room temperature to 200 °C and obtained the mapping of the thermal runaway. Can-Yong et al. reported and compared thermal runaway hazards of $LiCoO_2$ and $Li(Ni_{1/3}Co_{1/3}Mn_{1/3})O_2$ 18650 Li-ion batteries from room temperature to 300 °C by employing VSP2 [7]. The temperature and pressure characteristics were measured and analyzed. Feng et al. evaluated the thermal runaway features of a 25 Ah $Li(Ni_xCo_yMn_z)$-O_2/graphite prismatic battery using the extended volume-ARC (EV-ARC) [21]. The temperature ranges for different stages of thermal runaway was clarified, and the highest temperature inside the battery was measured as 870 °C. These work provide useful interpretation of thermal behaviours of Li-ion batteries, such as the temperature characteristics, impedance variation and heat variation when the battery is cycling. However, the complex thermal runaway process of a full cell have not been analyzed based on the cascading thermal reactions between the battery materials. Determination of detailed enthalpy released during the runaway process under high temperature and identification of these reactions and reaction kinetics have not been conducted. Furthermore, note that ARC and VSP2 cannot be applied to detect endothermic reaction, so DSC and C80 would be more suitable when endothermic process happen to the test object. C80 microcalorimeter provides the real-time change of heat flow and temperature of test object like DSC, and it presents better accuracy on detection of both exothermic and endothermic effects. The adiabatic environment formed in the calorimeter can maintain constant temperature stability ±0.1 °C, achieving a detectable heat flow of at least 0.1 μW. The high pressure vessel used for C80 can be sealed under high pressure, preventing the possible leak of test object, with the vessel volume as high as 12.5 ml. Based on the high accuracy, good tightness and big vessel volume, C80 was employed in this study to study the complex thermal behaviours of full cell system. However, when the test object is composed of many materials, such as the full cell, thermal runaway reactions always combine together and are difficult to separate and characterize from the results of thermal calorimeters with overlapped peaks. Deconvolution is a powerful mathematical method, which is often used to separate the combined peaks to capture clear and detailed peaks of a graph [22]. A deconvolution-based peak separation method is proposed to separate the overlapped thermal plot peaks obtained from C80 experiments in this paper.

Using this method, thermal plots of half and full Li-ion cells with multi-peaks are divided. Based on the deconvoluted data, separated thermal kinetics and reason of each deconvoluted peak is analysed. Thermal reactions of materials of a full cell at different mass ratios and heating rates are clearly distinguished. The dominant part of heat generation for the system is determined. Compared with the kinetics from the raw data, it is shown that this method is beneficial to reveal the reaction kinetics for the

complicated thermal runaway reactions occurring in the Li-ion battery. By employing the kinetics, the outcome of thermal events in abuse testing can be predicted, and the manufacturers can cut out a great deal of abuse tests, which would be costly, dangerous and time consuming [23,24].

2. Method

As we all know, an imperfect measuring instrument normally causes distortion or smearing or overlapping or broadening of peaks in an experimental graph. Deconvolution is a powerful mathematical method, which is often applied to remove the instrument response function. The combined and distorted peaks obtained from an experiment can be separated using a deconvolution method.

To deconvolute C80 or DSC heat flow curve, it is generally assumed that the recorded signal $f(t)$ is the "true" signal $g(t)$ convolved with the instrument response function $I(t)$:

$$f(t) = g(t) \otimes I(t) \qquad (1)$$

where $\otimes$ indicates convolution:

$$f(t) = g(t) \otimes I(t) = \int_{-\infty}^{+\infty} g(t-x)I(x)dx = \int_{-\infty}^{+\infty} g(x)I(t-x)dx \qquad (2)$$

The convolution theorem states that the Fourier transform of a convolution of two functions is the product of the Fourier transforms of the two individual functions:

$$\mathcal{F}[g(t) \otimes I(t)] = \mathcal{F}[g(t)] \times \mathcal{F}[I(t)] \qquad (3)$$

and then

$$\mathcal{F}[g(t)] = \mathcal{F}[g(t) \otimes I(t)]/\mathcal{F}[I(t)] = \mathcal{F}[f(t)]/\mathcal{F}[I(t)] \qquad (4)$$

where $\mathbf{F}$ indicates the operation of Fourier transformation:

$$\mathcal{F}[f(t)] = \int_{-\infty}^{+\infty} f(t)e^{-i\varpi t}dt \qquad (5)$$

and $\mathbf{F}^{-1}$ denotes inverse Fourier transformation:

$$\mathcal{F}^{-1}[F(x)] = \frac{1}{2\pi} \int_{-\infty}^{+\infty} F(x)e^{i\varpi x}dx \qquad (6)$$

After performing an inverse Fourier transform on each side of the Eq. (4), the function $f(t)$ is deconvoluted with $I(t)$, and the "true" signal $g(t)$ is obtained:

$$g(t) = f(t)[\otimes^{-1}]I(t) = \mathcal{F}^{-1}\{\mathcal{F}[g(t)]\} = \mathcal{F}^{-1}\{\mathcal{F}[f(t)]/\mathcal{F}[I(t)]\} \qquad (7)$$

where $\otimes^{-1}$ indicates deconvolution.

For a good deconvolution of overlapping peaks in molecular spectroscopy and scanning microcalorimetry of protein solutions, a Gaussian function is always used as the function $I(t)$ [25]:

$$f(x) = a_0 \exp\left[-\frac{1}{2}\left(\frac{x-a_1}{a_2}\right)^2\right] \qquad (8)$$

where x represents the temperature, $f(x)$ is the measured heat flux, a_0 is the peak amplitude, a_1 is the value of x corresponding to the peak centre and a_2 indicates the peak width.

It is supposed the single peaks have an asymmetrical shape, so an exponentially modified Gaussian (EMG) function is used in this work:

$$f(x) = \frac{a_0}{2a_3} \exp\left(\frac{a_2^2}{2a_3^2} + \frac{a_1 - x}{a_3}\right)\left[\text{erf}\left(\frac{x-a_1}{\sqrt{2}a_2} - \frac{a_2}{\sqrt{2}a_3}\right) + \frac{a_3}{|a_3|}\right] \qquad (9)$$

where a_3 is an asymmetry factor and erf() represents an error function. This type of distribution has been used in chromatographic applications [26–28]. The approach presented here has been applied to deconvolution of overlapping peaks in HPLC and

DSC [25], and appears to be used to C80 microcalorimeter in this paper.

By using the deconvolution method, the overlapping peaks are separated into several individual peaks. The complex reactions of the battery materials can be separated into several parts correspondingly. Then the kinetics and thermal dynamic of each part can be analyzed elaborately as the following Eq. (10), instead of the calculation of the entire complex reactions.

Assuming the reaction mechanism is dependent on the Arrhenius law, Eq. (10) is obtained:

$$\ln\left(\frac{dH/dt}{m\Delta H}\right) = -\frac{E}{R} \cdot \frac{1}{T} + \ln A \tag{10}$$

where dH/dt is heat flow obtained from the C80 data, E is activation energy, R is gas constant, T is temperature of system, A is pre-exponential factor, m is mass of reactant and $m\Delta H$ is the heat of reaction as Eq. (11):

$$m\Delta H = \int_{t_{initial}}^{t_{end}} (dH/dt)dt \tag{11}$$

where t_{end} is the end time of reaction, $t_{initial}$ is the initial time of reaction.

As shown in Fig. 1, activation energy E and pre-exponential factor A can be easily obtained by plotting the curve of $\ln(\frac{dH/dt}{m\Delta H})$ versus $-T^{-1}$.

3. Experimental

The highly purified organic solvents ethylene carbonate (EC), diethyl carbonate (DEC) were produced by Zhangjiagang Guotai-Huarong New Chemical Materials Co., Ltd. with the water content below 20 ppm. The salt LiPF$_6$ was commercially made by Tianjin Jinniu Power Sources Material Co. The electrolyte of 1.0 M LiPF$_6$/EC + DEC (1:1 wt.%) was prepared in an argon-filled glove box (MBraun Labmaster 130, <1 ppm O$_2$ and H$_2$O). The Celgard 2400 polyethylene was cut as 18 mm diameter separators. The positive electrode was made of 88% LiCoO$_2$ (Tianjin Bamo Co., Ltd.), 6% acetylene black, and 6% polyvinylidene fluoride (PVDF) binder. The negative electrode was made of 94% graphite material (Hongyuan Carbon Industry Co., Ltd.) and 6% PVDF binder. The electrodes were dried overnight in vacuum at 80 °C and handled in an argon filled glove box. The electrodes were cut as a 16 mm diameter disks with 400 or 800 μm thickness. For the CR2032 half cells (Li$_x$CoO$_2$/Li and Li$_x$C$_6$/Li), only 400 μm electrode disks were used, with lithium as counter electrode. In the case of full cells (Li$_x$CoO$_2$/Li$_x$C$_6$), the 800 μm electrode disks were also used when a higher mass of electrode material was required. In order to obtain the specific mass of different battery materials, all of the composition of the full cell (cell shell, electrode disks, electrolyte and separator) were weighed before or during the assembling.

The CR2032 coin cells were assembled in an argon-filled glove box as Ref. [29]. The Li$_x$CoO$_2$/Li half cells, Li$_x$C$_6$/Li half cells and Li$_x$CoO$_2$/Li$_x$C$_6$ full cells were galvanostatically cycled three times between 2.8–4.2 V, 0–3 V and 2.8–4.2 V, respectively, with 0.2 mA cm^{-2} current density on a multi-channel battery cycler (Neware BTS-6V10 mA, Shenzhen) at room temperature. For the third cycle, a constant voltage charging or discharging was performed by using constant current condition to stabilize the electrode to the desired voltage: 4.2 V for the Li$_x$CoO$_2$/Li half cells and Li$_x$CoO$_2$/Li$_x$C$_6$ full cells, 0 V for the Li$_x$C$_6$/Li half cells. From the cathode (or anode) mass, the constant current, and the time of current flow, the x of Li$_x$CoO$_2$ and Li$_x$C$_6$ was calculated as about 0.5 and 0.9, respectively.

Samples for different thermal analysis were composed of different materials with different mass ratios. In view that the higher
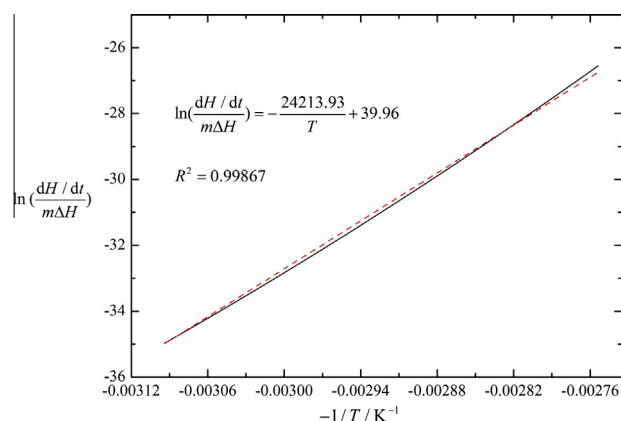

Fig. 1. Thermal-kinetic parameters estimated from relation between $\ln(\frac{dH/dt}{m\Delta H})$ and $-T^{-1}$.

mass ratio between electrolyte and electrode is apt for the research on the interaction between the transition metal ions dissolved from the cathodes and the electrolyte [30], the higher content electrolyte was adopted as the following mass ratio: Li$_x$CoO$_2$ or Li$_x$C$_6$: electrolyte = 1:2.2. On the other hand, in the case of the real commercial Li-ion battery, the mass ratio of electrolyte to electrode is lower. For example, an 18,650 Li-ion battery comprises about 12–14 g of the positive electrode, 5–6 g of the carbon electrode, and 4–5 g of the electrolyte. Therefore, the following mass ratio between electrode and electrolyte was also investigated: Li$_x$CoO$_2$: electrolyte = 2.5:1 and Li$_x$C$_6$: electrolyte = 1:1. For the study on the thermal performance of full cells, samples were some composed of different mass of battery materials. The specific mass would be described in Section 4.4.

In order to obtain the sample with different mass, the cycled cells were disassembled in the glove box. In the case of half cells, dimethyl carbonate (DMC) was used to rinse the electrolyte from the electrode. The electrode material Li$_x$CoO$_2$ or Li$_x$C$_6$ was dried to remove DMC and then scraped from the current collectors carefully. The dried electrode material and electrolyte with specific mass were eventually added into the C80 high-pressure vessel to perform the thermal analysis test. For the disassembled full cells, as shown in Fig. 2, the cell core was taken out and folded carefully using insulated forceps. The folded cell core was then put into a sample holder. The mass of disassembled cell shell was compared to the mass recorded before the cell assembling. The difference between these two values was determined as the mass of the electrolyte attached on the cell shell. The same mass electrolyte was added into the cell core to ensure that all of the materials in the cell shell were in the sample holder already. Finally, the sample holder was embedded in the high-pressure C80 vessel (proof pressure of 100 atm), which was then sealed in the argon atmosphere using two special wrenches under high pressure (4 ± 3 mbar higher than the atmospheric pressure), preventing the possible leak of test object. After the above preparation, thermal analysis test was operated based on a C80 micro-calorimeter. The weight of each sample (vessel + sample) was measured before and after the experiment to verify whether the system was hermetically sealed or not. The measurements were carried out using a heating rate 0.2 °C min^{-1} in the temperature range 30–300 °C.

4. Results and discussions

4.1. Electrolyte thermal analysis

Fig. 3 shows the initial heat flow plot and the corresponding deconvoluted plots of 1.0 M LiPF$_6$/EC + DEC electrolyte at
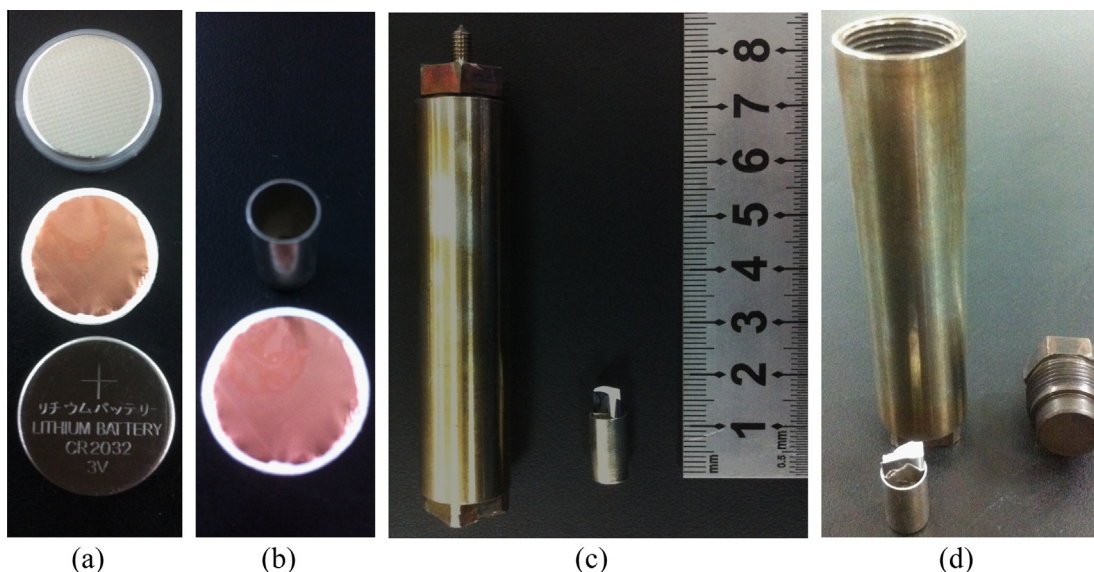
Fig. 2. Schematic diagram of the preparation of C80 thermal analysis on the full cell: (a) CR2032 cell shell and cell core, which is composed of positive and negative electrodes, separator and electrolyte; (b) the cell core taken out from the dissembled cell, and the sample holder with 0.6 cm diameter and 1.3 cm height; (c) the C80 high pressure vessel and the sample holder with folded cell core; and (d) the sample holder would be put into the C80 vessel.
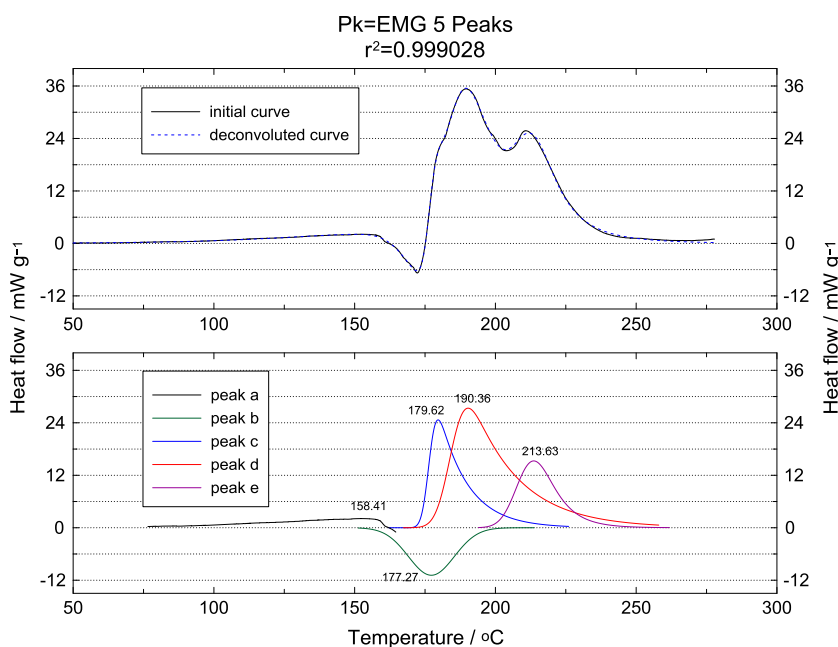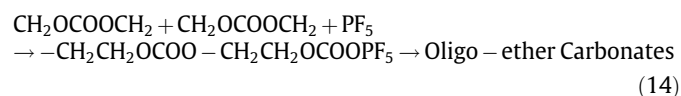

Fig. 3. Initial and deconvoluted C80 curves of heat flow versus temperature of 1.0 M $LiPF_6$/EC + DEC electrolyte at 0.2 °C min^{-1} heating rate.
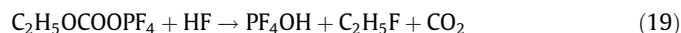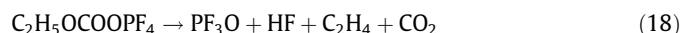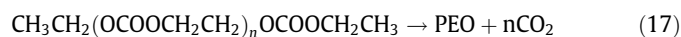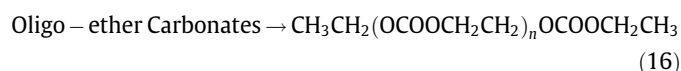
0.2 °C min^{-1} heating rate. The solid line is the initial heat flow curve obtained from C80 microcalorimeter. The dotted line is the deconvoluted plot composed of five deconvoluted peaks (peaks a–e). Before deconvolution, one endothermic peak and two exothermic peaks were obviously observed. After deconvolution, two more exothermic peaks were picked from the plots. Peak a shows that the electrolyte starts to react near 75 °C. Then the electrolyte shows a slow exothermic process and reaches the peak temperature at 158 °C with heat generation of −55.11 J g^{-1}. This peak should be owing to the generation of the strong Lewis acid PF_5 and the reaction between PF_5 and the trace water:

$$LiPF_6 \rightarrow LiF + PF_5 \qquad (12)$$

$$PF_5 + H_2O \rightarrow PF_3O + 2HF \qquad (13)$$

Peak b shows an endothermic process with the peak temperature at 177.27 °C. The heat absorption of this peak is 67.71 J g^{-1}. This process is identified as the Lewis acid-catalyzed ring-opening reaction of EC ($CH_2OCOOCH_2$) [31] and the elimination reaction of DEC ($C_2H_5OCOOC_2H_5$) in the presence of PF_5 [32,33]:

$$CH_2OCOOCH_2 + CH_2OCOOCH_2 + PF_5$$
$$\rightarrow -CH_2CH_2OCOO - CH_2CH_2OCOOPF_5 \rightarrow Oligo - ether\ Carbonates$$
$$(14)$$

$$C_2H_5OCOOC_2H_5 + PF_5 \rightarrow C_2H_5OCOOPF_4 + HF + C_2H_4 \qquad (15)$$

With a rise of temperature, the products of the above reactions sustain further complex reactions [17], as the following equations:

$$Oligo-ether\ Carbonates \rightarrow CH_3CH_2(OCOOCH_2CH_2)_nOCOOCH_2CH_3 \tag{16}$$

$$CH_3CH_2(OCOOCH_2CH_2)_nOCOOCH_2CH_3 \rightarrow PEO + nCO_2 \tag{17}$$

$$C_2H_5OCOOPF_4 \rightarrow PF_3O + HF + C_2H_4 + CO_2 \tag{18}$$

$$C_2H_5OCOOPF_4 + HF \rightarrow PF_4OH + C_2H_5F + CO_2 \tag{19}$$

$$C_2H_4 + HF \rightarrow C_2H_5F \tag{20}$$

These reactions overlap each other and generate heat violently as shown in peak c, d and e. A comparison of these three peaks shows that they have different heat generation but close exothermic peaks shape, which implies their thermal behaviours are similar. Thermodynamic and kinetic parameters of these deconvoluted peaks were summarized and listed in Table 1. The total heat generation integrated from the deconvoluted peaks is almost same as that of the initial one. The activation energy calculated based on peak a is close to that calculated from the beginning of the initial plots. The consistency supports the reasonability of the deconvolution method used in this work. Moreover, not only the thermal dynamic and kinetic parameters of the early reactions, parameters of the following reactions at elevated temperature can also be obtained using the deconvolution method: the total reaction process can be analyzed in detail.

4.2. Electrolyte-Li_xCoO_2 thermal analysis

Fig. 4 shows the initial heat flow plot and the corresponding deconvoluted plots of Li_xCoO_2 and 1.0 M $LiPF_6$/EC + DEC electrolyte at 1:2.2 mass ratio at 0.2 °C min^{-1} heating rate. Using deconvolution method, five exothermic peaks were picked from the plots, which were designated as peak a, b, c, d, and e. Peak a shows the system generates heat moderately near 60 °C, which is considered as the decomposition of some thermally unstable substances formed on the cathode surface. The unstable substances should be the products of the electrolyte oxidized by the charged cathode. Their thermally unstable properties should be like the SEI formed on the surface of the negative material [18]. Peak b shows the reaction rate begins to increase after a small thermal fluctuation. Note that there is some discrepancy between the initial and deconvolution curves near 150 °C, which should be result from the endothermic effect of the abundant electrolyte in the sample system. After this discrepancy, the system reaches the peak temperature at 164.24 °C, with heat generation of −290.80 J g^{-1}. This peak is considered as the disproportionation of the charged $LiCoO_2$:

Table 1
Thermodynamics and kinetics of 1.0 M $LiPF_6$/EC + DEC electrolyte at 0.2 °C min^{-1} heating rate.

Electrolyte	Onset temp. (°C)	Peak temp. (°C)	Reaction heat (J g^{-1})	Activation energy E (kJ mol^{-1})	Pre-exponential factor A (s^{-1})	Relativity R^2
Initial	75.58	172, 188, 211	35.6, 412.6	218.53	5.54×10^{20}	0.983
Peak a	75.58	158.41	−55.11	201.31	2.27×10^{17}	0.998
Peak b	160.43	177.27	67.71	–	–	–
Peak c	171.04	179.62	−114.00	972.65	5.07×10^{98}	0.996
Peak d	176.62	190.36	−243.79	742.87	5.75×10^{95}	0.993
Peak e	198.91	213.63	−89.55	496.11	1.91×10^{46}	0.998
Total	–	–	−384.74	–	–	–
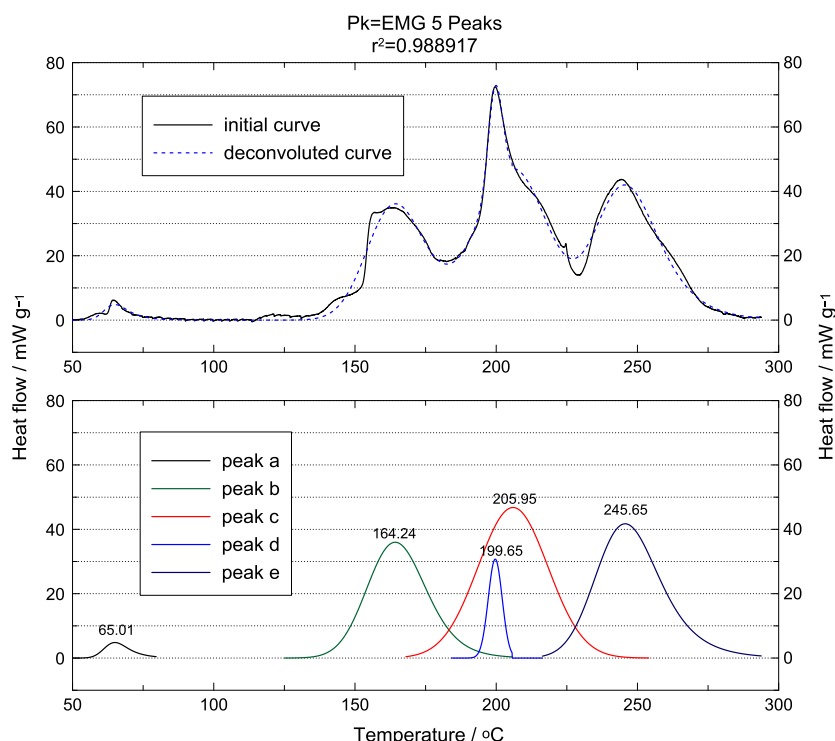
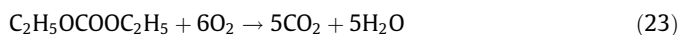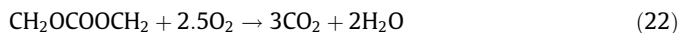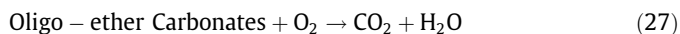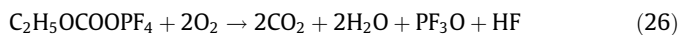**Fig. 4.** Initial and deconvoluted C80 curves of heat flow versus temperature of Li_xCoO_2 and 1.0 M $LiPF_6$/EC + DEC electrolyte at 1:2.2 mass ratio at 0.2 °C min^{-1} heating rate.

$$Li_xCoO_2 \rightarrow xLiCoO_2 + \frac{1}{3}(1-x)Co_3O_4 + \frac{1}{3}(1-x)O_2 \qquad (21)$$
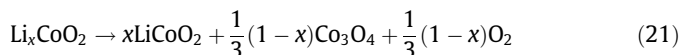
Since the mass ratio of Li_xCoO_2 and electrolyte is 1:2.2, plenty of electrolytes generate heat and gas violently from 170 °C. Meanwhile, oxygen is accumulating as Eq. (21), so the pressure and temperature of the system is becoming higher. In such conditions, the solvents react with oxygen and generate heat as shown in peak c:

$$CH_2OCOOCH_2 + 2.5O_2 \rightarrow 3CO_2 + 2H_2O \qquad (22)$$

$$C_2H_5OCOOC_2H_5 + 6O_2 \rightarrow 5CO_2 + 5H_2O \qquad (23)$$

When the temperature is up to 191.39 °C, charged $LiCoO_2$ decomposes further and releases more oxygen, which oxidizes the thermal decomposition products of electrolyte and generates more heat. The corresponding thermal behaviours appear as peak d and peak e:

$$Co_3O_4 \rightarrow 3CoO + 0.5O_2 \qquad (24)$$

$$CoO \rightarrow Co + 0.5O_2 \qquad (25)$$

$$C_2H_5OCOOPF_4 + 2O_2 \rightarrow 2CO_2 + 2H_2O + PF_3O + HF \qquad (26)$$

$$Oligo - ether\ Carbonates + O_2 \rightarrow CO_2 + H_2O \qquad (27)$$

Thermodynamic and kinetic parameters of these deconvoluted peaks were summarized and listed in Table 2. The heat generated by peak c is the largest compared with other peaks, which means the oxidization of solvents is a major contribution to the heat generation of the system. However, the lower electrolyte containing system shows different thermal behaviours. Fig. 5 shows the initial heat flow plot and the corresponding deconvoluted plots of Li_xCoO_2 and 1.0 M $LiPF_6/EC + DEC$ electrolyte at 2.5:1 mass ratio at 0.2 °C min^{-1} heating rate. After deconvolution method, four exothermic peaks were picked from the plots, which were designated as peak a, b, c, and d. Thermodynamic and kinetic parameters of these deconvoluted peaks were summarized and listed in Table 3.

Compared with Fig. 4, the mild exothermic process near 60 °C does not show up when the mass ratio between Li_xCoO_2 and electrolyte is 2.5:1. It can be speculated that the unstable substance formed on the cathode surface is relevant to the electrolyte. When the electrolyte is not too much, formation of the unstable substance is little. Then the corresponding exothermic process at elevated temperature becomes mild and slow, as shown in peak a: the system starts to release heat at 103.83 °C, and reaches the peak temperature at 135.11 °C with heat generation of -77.58 J g^{-1}.

As the temperature grows, the system begins to release heat clearly, as shown in peak b. The exothermic process of peak b is from 151.74 °C to 212.81 °C, which incorporates the disproportionation and the further decomposition of charged $LiCoO_2$. That is why the peak d corresponding to the decomposition of charged $LiCoO_2$ in Fig. 4 does not arise in Fig. 5.

Peak c shows exothermic behaviour from 177.62 °C, its temperature range and activation energy (Table 3) is close to that of the peak c in Fig. 4. This peak is considered as the reaction between oxygen and solvents. But when the mass ratio of Li_xCoO_2 and electrolyte is 2.5:1, less solvents causes less heat generation and lower pre-exponential factor.

Table 2
Thermodynamics and kinetics of Li_xCoO_2 and 1.0 M $LiPF_6/EC + DEC$ electrolyte at 1:2.2 mass ratio at 0.2 °C min^{-1} heating rate.

Li_xCoO_2-electrolyte 1:2.2	Onset temp. (°C)	Peak temp. (°C)	Reaction heat (J g^{-1})	Activation energy E (kJ mol^{-1})	Pre-exponential factor A (s^{-1})	Relativity R^2
Peak a	60.37	65.01	−18.31	241.92	9.55×10^{33}	0.993
Peak b	131.52	164.24	−305.09	420.53	3.52×10^{47}	0.979
Peak c	171.85	205.95	−462.45	493.44	1.47×10^{52}	0.994
Peak d	191.39	199.65	−59.92	670.09	1.02×10^{132}	0.968
Peak e	216.44	245.65	−383.28	630.85	3.65×10^{62}	0.978
Total	–	–	−1229.05	–	–	–

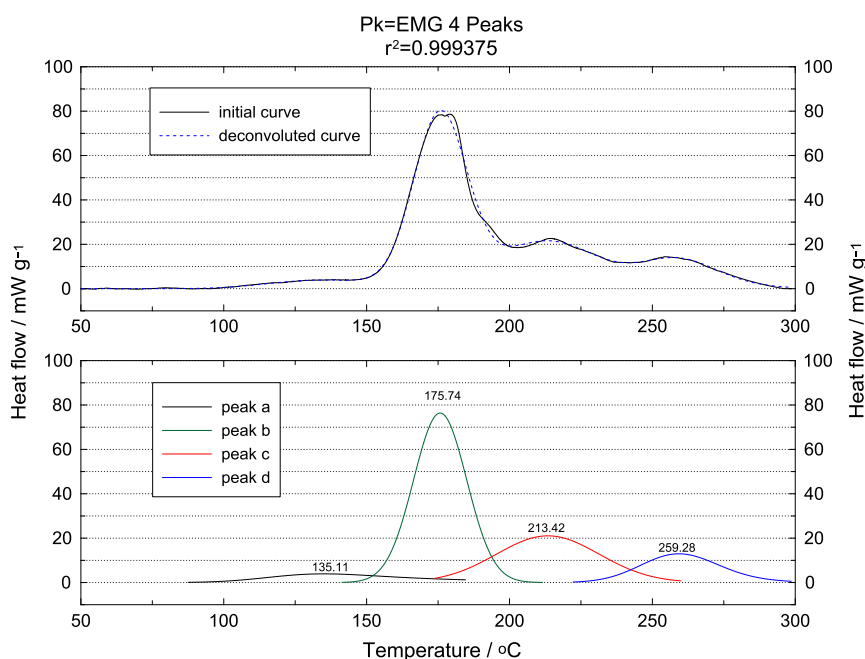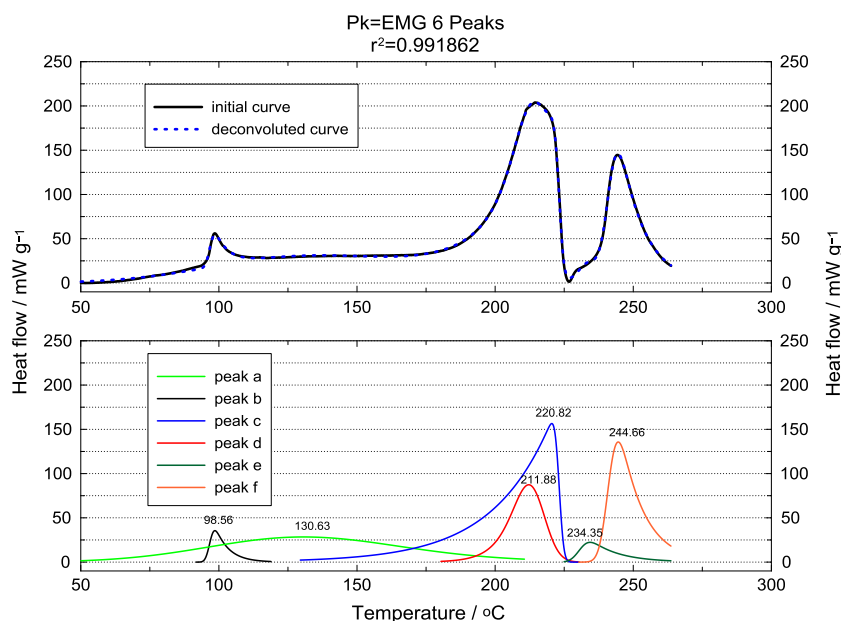**Fig. 5.** Initial and deconvoluted C80 curves of heat flow versus temperature of Li_xCoO_2 and 1.0 M $LiPF_6/EC + DEC$ electrolyte at 2.5:1 mass ratio at 0.2 °C min^{-1} heating rate.

Table 3
Thermodynamics and kinetics of Li_xCoO_2 and 1.0 M $LiPF_6$/EC + DEC electrolyte at 2.5:1 mass ratio at 0.2 °C min^{-1} heating rate.

| Li_xCoO_2-electrolyte 2.5:1	Onset temp. (°C)	Peak temp. (°C)	Reaction heat ($J\,g^{-1}$)	Activation energy E (kJ mol^{-1})	Pre-exponential factor A (s^{-1})	Relativity R^2
Peak a	103.83	135.11	−51.8	153.64	1.5×10^{16}	0.964
Peak b	149.74	175.74	−484	389.93	9.15×10^{33}	0.962
Peak c	177.62	213.42	−268	482.68	5.14×10^{27}	0.980
Peak d	226.95	259.28	−131	712.43	1.57×10^{68}	0.993
Total	–	–	−934	–	–	–

Fig. 6. Initial and deconvoluted C80 curves of heat flow versus temperature of Li_xC_6 and 1.0 M $LiPF_6$/EC + DEC electrolyte at 1:2.2 mass ratio at 0.2 °C min^{-1} heating rate.

Peak d in Fig. 5 appears like peak e in Fig. 4, it shows less heat generation and higher activation energy. The difference between the last two peaks in Fig. 5 and those in Fig. 4 shows that the oxidization of solvents and decomposition products of electrolyte reduce with the decrease of the electrolyte content.

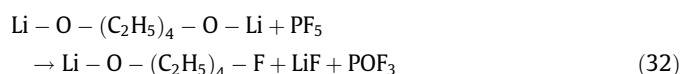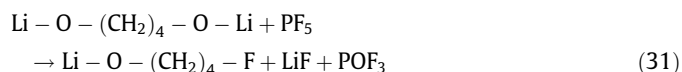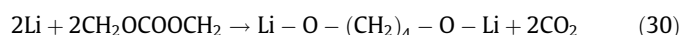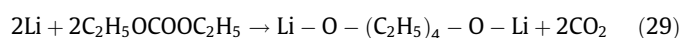### 4.3. Electrolyte-Li_xC_6 thermal analysis

Fig. 6 shows the initial heat flow plot and the corresponding deconvoluted plots of Li_xC_6 and 1.0 M $LiPF_6$/EC + DEC electrolyte at 1:2.2 mass ratio at 0.2 °C min^{-1} heating rate. After deconvolution, six exothermic peaks were picked from the plots, which were designated as peak a, b, c, d, e and f. Thermodynamic and kinetic parameters of these deconvoluted peaks were summarized and listed in Table 4.

Peak a releases heat from 64.28 °C, its beginning behaviour is similar to that of the electrolyte in Fig. 3. This peak is mainly caused by the thermal decomposition of the electrolyte. As the temperature builds up, peak b releases heat from 93.57 °C and reaches peak temperature at 98.56 °C with heat generation of −84.99 J g^{-1}. This exothermic process is the breakdown of SEI layer formed on the surface of negative material. The SEI layer mainly consists of stable (such as Li_2CO_3, LiF) and metastable components (such as polymers, $(CH_2OCOOLi)_2$, ROCOOLi and ROLi) [34–39]. The metastable components decompose at 90–120 °C as following [34]:

$$(CH_2OCO_2Li)_2 \rightarrow Li_2CO_3 + C_2H_4 + CO_2 + \frac{1}{2}O_2 \quad (28)$$
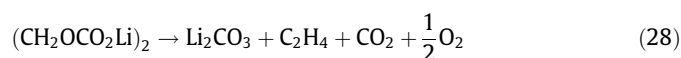
The breakdown of SEI causes the intercalated lithium in the negative material to react directly with the organic solvents used

in the electrolyte [34], which is shown as peak c and the following equations:

$$2Li + 2C_2H_5OCOOC_2H_5 \rightarrow Li - O - (C_2H_5)_4 - O - Li + 2CO_2 \quad (29)$$

$$2Li + 2CH_2OCOOCH_2 \rightarrow Li - O - (CH_2)_4 - O - Li + 2CO_2 \quad (30)$$

$$Li - O - (CH_2)_4 - O - Li + PF_5$$
$$\rightarrow Li - O - (CH_2)_4 - F + LiF + POF_3 \quad (31)$$

$$Li - O - (C_2H_5)_4 - O - Li + PF_5$$
$$\rightarrow Li - O - (C_2H_5)_4 - F + LiF + POF_3 \quad (32)$$

Peak d releases heat from 182.72 °C to 211.88 °C, with heat generation of −431.70 J g^{-1}. The temperature range is close to that of the peak d and peak e in Fig. 3. If the heat generation was calculated based on the mass of electrolyte, the value would be −179.88 J g^{-1}. This value should be owing to the total heat generation of peak e in Fig. 3 (−89.55 J g^{-1}) and some heat generation of peak d in Fig. 3. Therefore, peak d in Fig. 6 is believed to be caused by the decomposition of the abundant electrolyte in the system.

The stable LiF generated by $LiPF_6$ as Eq. (12) and the products caused by Eqs. (29)–(32) deposit on the surface of Li_xC_6, form the new SEI and inhibit the reactivity of Li_xC_6. That is why the system shows a short halt on the heat release near 225 °C. The formation of new SEI stops when either the new layer is thick enough to insulate reactants or all the intercalated Li has been consumed [11]. When the temperature is above 230 °C, the unstable components of the new SEI layer decompose [40]. The corresponding reactions contribute peak e, which shows a small heat generation and modest thermal behaviour.

Table 4
Thermodynamics and kinetics of Li_xC_6 and 1.0 M $LiPF_6$/EC + DEC electrolyte at 1:2.2 mass ratio at 0.2 °C min^{-1} heating rate.

Li_xC_6-electrolyte 1:2.2	Onset temp. (°C)	Peak temp. (°C)	Reaction heat (J g^{-1})	Activation energy E (kJ mol^{-1})	Pre-exponential factor A (s^{-1})	Relativity R^2
Peak a	64.28	130.63	−288.28	59.73	9166.68	0.998
Peak b	93.57	98.56	−84.99	277.01	3.32×10^{41}	0.966
Peak c	133.94	220.82	−1175.80	71.157	3378.27	0.993
Peak d	182.72	211.88	−401.70	290.85	3.15×10^{28}	0.991
Peak e	226.81	234.35	−106.65	771.22	2.51×10^{127}	0.998
Peak f	237.35	244.66	−588.45	905.05	3.10×10^{125}	0.989
Total	–	–	−2645.87	–	–	–
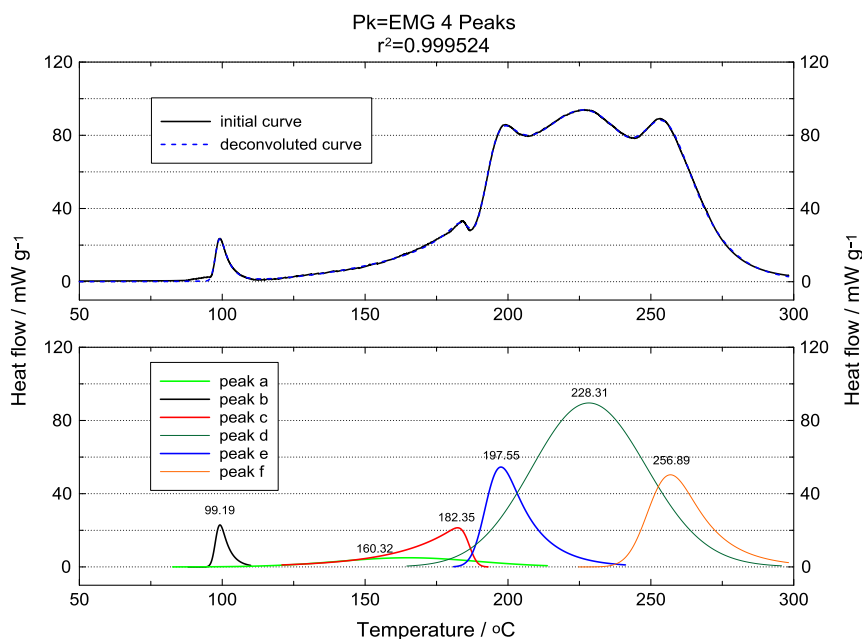
Fig. 7. Initial and deconvoluted C80 curves of heat flow versus temperature of Li_xC_6 and 1.0 M $LiPF_6$/EC + DEC electrolyte at 1:1 mass ratio at 0.2 °C min^{-1} heating rate.

As PVDF was used when the electrode was made, it could be dehydrofluorinated in the presence of the electrolyte as the acidic medium as follows [41]:
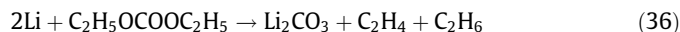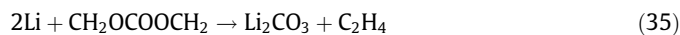
$$-CH_2CF_2- \rightarrow base \rightarrow -CH=CF- +HF \tag{33}$$

$$Li + HF \rightarrow LiF + H_2 \tag{34}$$
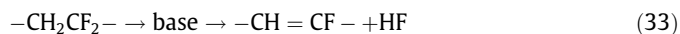
It is considered that peak f occurring above 235 °C is caused by these reactions.

Fig. 7 shows the initial heat flow plot and the corresponding deconvoluted plots of Li_xC_6 and 1.0 M $LiPF_6$/EC + DEC electrolyte at 1:1 mass ratio at 0.2 °C min^{-1} heating rate. After deconvolution, six exothermic peaks were picked from the plots, which were designated as peak a, b, c, d, e and f. Thermodynamic and kinetic parameters of these deconvoluted peaks were summarized and listed in Table 5.

In contrast with the peak a in Fig. 6, peak a in Fig. 7 shows a higher onset and peak temperature with a lower heat generation, which is consequent on the less electrolyte in the system. The temperature range and peak shape of peak b indicate that this peak is attributed to the thermal decomposition of the SEI layer. In addition, the less heat generation shows that the metastable components of the SEI layer decrease as the contents of electrolyte decrease.

Peak c shows an approximate onset temperature but a lower peak temperature and heat generation compared with peak c in Fig. 6. It is like a smaller version of peak c in Fig. 6. This phenomenon should be caused by the lower electrolyte content.

Peak d releases heat from 167.25 °C and reaches peak at 228.31 °C. The broad and high peak shows large heat generation of −1349.98 J g^{-1}. Its thermal behaviour is quite different to that of the peak d in Fig. 6. Since the mass ratio of Li_xC_6 and electrolyte is 1:1 rather than 1:2.2 and the electrolyte is consumed in previous reactions, peak d should be attributed to the reactions dominated by the intercalated lithium in Li_xC_6. The possible reactions should be like follows [34]:

$$2Li + CH_2OCOOCH_2 \rightarrow Li_2CO_3 + C_2H_4 \tag{35}$$

$$2Li + C_2H_5OCOOC_2H_5 \rightarrow Li_2CO_3 + C_2H_4 + C_2H_6 \tag{36}$$

The above products Li_2CO_3 and the LiF generated by $LiPF_6$ as Eq. (12) form the new SEI layer. Since Li_2CO_3 and LiF are very stable, the decomposition of the new SEI does not occur as peak e in Fig. 6. Peak e in Fig. 7 generates heat from 180.36 °C and reaches the peak temperature at 197.55 °C, with a heat generation of −316.15 J g^{-1}. Its temperature range and heat generation are very close to that of the peak c and peak d in Fig. 3, so peak e is thought to be the thermal decomposition of the electrolyte. Compared with the peak f in Fig. 6, peak f in Fig. 7 shows an approximate thermal behaviour, which is caused by the reaction between Li and PVDF as Eqs. (33) and (34), but the heat generation here is less than that of the peak f in Fig. 6.

In general, when the mass ratio of the electrode and electrolyte changes from 1:2.2 to 1:1, the deconvoluted peaks a, b, c and f do not show any change except some decreased heat generation, increased activation energy and increased onset or peak

Table 5
Thermodynamics and kinetics of Li_xC_6 and 1.0 M $LiPF_6$/EC + DEC electrolyte at 1:1 mass ratio at 0.2 °C min^{-1} heating rate.

Li_xC_6-electrolyte 1:1	Onset temp. (°C)	Peak temp. (°C)	Reaction heat (J g^{-1})	Activation energy E (kJ mol^{-1})	Pre-exponential factor A (s^{-1})	Relativity R^2
Peak a	87.93	160.32	−91.10	128.61	1.38×10^{12}	0.998
Peak b	94.52	99.19	−38.67	665.39	3.79×10^{88}	0.966
Peak c	128.04	182.35	−164.37	85.53	3759.65	0.991
Peak d	167.25	228.31	−1349.98	371.71	3.35×10^{38}	0.998
Peak e	180.36	197.55	−316.15	1091.68	2.69×10^{163}	0.993
Peak f	235.71	256.89	−375.65	919.08	9.02×10^{150}	0.989
Total	–	–	−2335.93	–	–	–

Table 6
Thermodynamics and kinetics of full cell A at 0.2 °C min^{-1} heating rate.

	Onset temp. (°C)	Peak temp. (°C)	Reaction heat (mJ)	Reaction heat per gram* (J g^{-1})	Activation energy E (kJ mol^{-1})	Pre-exponential factor A (s^{-1})	Relativity R^2
Peak a	72.69	78.58	−315.84	−16.11	443.28	1.83×10^{76}	0.997
Peak b	92.15	106.69	−2077.67	−98.00	59.73	9235.42	0.998
Peak c	114.37	129.61	−1028.45	−48.51	71.15	3496.35	0.989
Peak d	126.66	131.45	1298.54	236.10			0.984
Peak e	141.39	157.06	−5194.19	–	521.79	8.17×10^{57}	0.986
Peak f	156.01	166.24	−3116.51	−159.01	489.34	1.15×10^{82}	0.990
Peak g	158.86	181.84	−10907.81	−556.52	478.62	2.61×10^{66}	0.989
Peak h	178.59	213.29	−24931.98	−1176.04	1091.88	1.92×10^{146}	0.984
Peak i	218.81	242.84	−7894.97	−402.80	828.98	6.53×10^{175}	0.986
Peak j	232.04	255.27	−10843.94	−511.51	381.03	2.40×10^{140}	0.984
Total	–	–	−65012.84	–	–	–	–

* Heat generation based on specific electrode.

4.4. Full cell thermal analysis

temperature. However, peak d and e in Fig. 6 are quite different from those in Fig. 7. The reactions between the intercalated lithium and the electrolyte change a lot. The thermal breakdown of the new SEI layer does not appear when the electrolyte is not much in the coexisting system.

Fig. 9 shows the initial heat flow plot and the corresponding deconvoluted plots of full cell A at 0.2 °C min^{-1} heating rate. The full cell A was composed of 19.6 mg Li_xCoO_2, 21.2 mg Li_xC_6, 45.1 mg 1.0 M $LiPF_6$/EC + DEC electrolyte, 5.5 mg separator, 11.2 mg aluminium foil and 18.0 mg copper foil. The mass ratio between the electrode and the electrolyte is about 1:2.2. The deconvoluted results of this figure can be compared to Figs. 4 and 6. After deconvolution, ten exothermic peaks were picked from the plots, which were designated as peak a, b, c, d, e, f, g, h, i and j. Thermodynamic and kinetic parameters of these peaks were summarized and listed in Table 6. As the system is composed of more than four kinds of materials, it is not reasonable to calculate the heat generation of the deconvoluted peak based on the mass of the electrode materials or electrolytes. The heat generation per gram of each peak is calculated based on the mass of the related specific electrode in the following analysis.

Peak a shows the system releases heat from 72.69 °C and reaches the peak at 78.58 °C with heat generation of −315.84 mJ. If the heat generation of this peak is divided by the mass of Li_xCoO_2, the heat generation per gram is obtained as −16.11 J g^{-1}, which is close to that of the peak a in Fig. 4 (−18.3 J g^{-1}). Therefore, peak a in Fig. 9 is assigned to the decomposition of the thermally unstable substances formed on the cathode surface. After peak a, peak b releases heat at 92.15 °C and reaches the peak at 106.69 °C. The heat generation of this peak (−2077.67 mJ) divided by the mass of Li_xC_6 equals to −98.00 J g^{-1}, which is almost similar to that of the SEI decomposition (−84.99 J g^{-1}) obtained from the peak b in Fig. 6. It can be seen that peak b is caused by the SEI decomposition.

With the increase in the temperature, peak c shows an exothermic behaviour with heat generation of −1028.45 mJ. The heat generation per gram can be determined as −48.51 J g^{-1} or 52.47 J g^{-1} based on the mass of Li_xC_6 or Li_xCoO_2, respectively. It is difficult to find a peak to match these values from the previous analysis. However, peak c appears from 114.37 °C with a peak temperature of 129.61 °C. The temperature range corresponds to the range of latter part of peak a in Fig. 4. Given that the electrolyte reacts with the positive and negative electrode materials at the same time, the electrolyte in this system is not enough to release heat at lower temperature. Therefore, peak c should be a part of the decomposition of the electrolyte. Within the close temperature range, peak d shows an endothermic behaviour with heat generation of 1298.54 mJ. From results in Fig. 8 and Table 7, the separator shows an approximate endothermic peak with a heat generation of 233.19 J g^{-1}. This value is same to the specific heat of peak d (236.10 J g^{-1}) calculated by dividing 1298.54 mJ by the mass of the separator, so peak d is attributed to the melting of the separator.

Peak e occurs from 141.39 °C with a peak temperature of 157.06 °C and heat generation of −5194.19 mJ. In comparison with the peaks in Figs. 4 and 6, it cannot be found a compatible peak for peak e from the standpoint of searching close heat generation or temperature range. Since peak e follows the melting behaviour of separator, the positive and negative electrode materials begin to contact each other with the increase of temperature. The short circuit between Li_xCoO_2 and Li_xC_6 then causes heat generation and possible reactions. This peak cannot be found in the previous half-cell coexisting system, but appears in the following two cases of full cells, which confirms the above speculation. Peak f shows a similar peak temperature with the peak b in Fig. 4. It implies that peak f is relevant with the disproportionation of Li_xCoO_2. However, peak f shows higher onset temperature and lower heat generation in contrast with peak b in Fig. 4. Affected by the previous peak e, Li_xCoO_2 should react with Li_xC_6 and be consumed, so its disproportionation is delayed and incomplete.

After peak f, a large peak shown as peak g appears from 158.86 °C to 209.53 °C, with peak temperature of 181.84 °C and
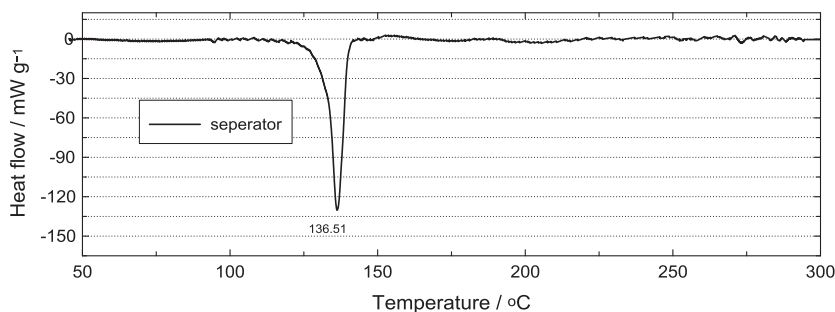
Fig. 8. Initial C80 curve of heat flow versus temperature of separator at 0.2 °C min⁻¹ heating rate.

Table 7
Thermodynamics and kinetics of separator at 0.2 °C min⁻¹ heating rate.

Separator	Onset temp. (°C)	Peak temp. (°C)	Reaction heat (J g⁻¹)
	121.78	136.51	233.19

heat generation of −10907.81 mJ. According to the similar temperature range, peak c and d in Fig. 4 should be the parallel peaks for peak g in Fig. 9. Furthermore, the sum of the heat generation of peak c ($-462.45\,\text{J g}^{-1}$) and d ($-59.92\,\text{J g}^{-1}$) in Fig. 4 is $-522.37\,\text{J g}^{-1}$. Based on the mass of Li_xCoO_2, the heat generation per gram of peak g can be identified as $-556.52\,\text{J g}^{-1}$. Therefore, peak g can be assigned to the decomposition of Li_xCoO_2 and the reactions between the released oxygen and the solvents. The peak temperature of peak h (213.29 °C) is close to that of the peak c in Fig. 6. By dividing −24931.98 mJ by the mass of Li_xC_6, the heat generation per gram of peak h is obtained as $-1176.04\,\text{J g}^{-1}$. It is similar to that of the heat generation of peak c ($-1175.80\,\text{J g}^{-1}$) in Fig. 6, so peak h in Fig. 9 is due to the reactions of the intercalated lithium in the negative material with the organic solvents.

Peak i shows the exothermic behaviour from 218.81 °C. Its peak temperature and heat generation is 242.84 °C and $-402.80\,\text{J g}^{-1}$ (based on the mass of Li_xCoO_2), respectively. In view of the onset temperature, peak temperature and heat generation of peak e in Fig. 4 are 216.44 °C, 245.65 °C and $-383.28\,\text{J g}^{-1}$, peak i in Fig. 9

is equivalent to this peak. Thus, peak i is consequent on the oxidation of the thermal decomposition products of electrolyte. Peak j releases heat from 232.04 °C and reaches the peak temperature at 255.27 °C. Its temperature range is close to that of peak f in Fig. 6. If the heat generation of peak j (−10843.94 mJ) is divided by the mass of Li_xC_6, the heat generation per gram of peak j is determined as $-511.51\,\text{J g}^{-1}$. It is also close to that of peak f ($-588.45\,\text{J g}^{-1}$) in Fig. 6, so peak j is triggered by the reactions related with PVDF.

From the above analysis, it can be found that the complex thermal behaviour of the full cell can be divided to several peaks. According to the previous study on the thermal dynamic characteristics of the half-cell system, the deconvoluted peaks of the full cell system can be distinguished as some specific reactions, and the detail thermal dynamic characteristics of each peak can also be obtained.

Fig. 10 shows the initial heat flow plot and the corresponding deconvoluted plots of full cell B at 0.2 °C min⁻¹ heating rate. The full cell B was composed of 60.1 mg Li_xCoO_2, 24.0 mg Li_xC_6, 23.8 mg 1.0 M $LiPF_6$/EC + DEC electrolyte, 4.2 mg separator, 11.2 mg aluminium foil and 18.0 mg copper foil. The mass ratios are about 2.5:1 for Li_xCoO_2: electrolyte and 1:1 for Li_xC_6: electrolyte, similar to the mass ratios of the 18,650 cell mentioned earlier and the cases of Figs. 5 and 7. After deconvolution, seven exothermic peaks were picked from the plots, which were designated as peak a, b, c, d, e, f and g. Thermodynamic and kinetic
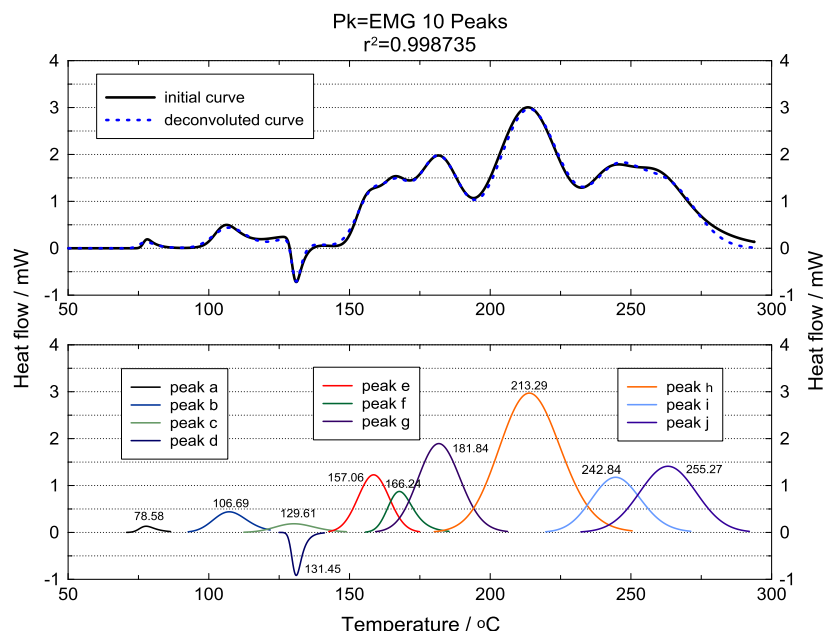

Fig. 9. Initial and deconvoluted C80 curves of heat flow versus temperature of full cell A at 0.2 °C min⁻¹ heating rate.
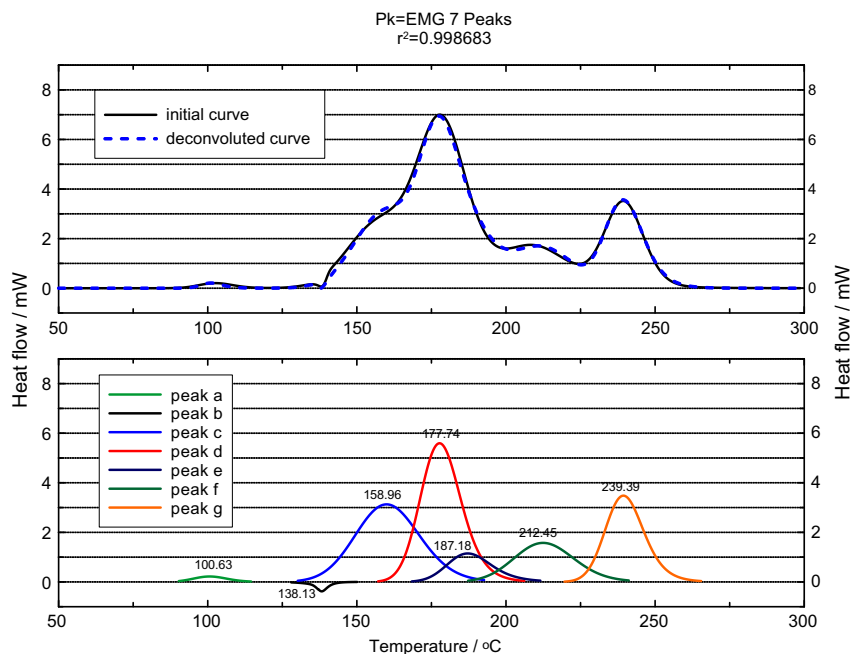
Fig. 10. Initial and deconvoluted C80 curves of heat flow versus temperature of full cell B at 0.2 °C min^{-1} heating rate.

Table 8
Thermodynamics and kinetics of full cell B at 0.2 °C min^{-1} heating rate.

	Onset temp. (°C)	Peak temp. (°C)	Reaction heat (mJ)	Reaction heat per gram* (J g^{-1})	Activation energy E (kJ mol^{-1})	Pre-exponential factor A (s^{-1})	Relativity R^2
Peak a	89.06	100.63	−1077.66	−44.90	130.40	2.53×10^{12}	0.994
Peak b	127.79	138.13	943.74	224.70	–	–	–
Peak c	129.35	158.96	−25615.66	–	557.23	3.61×10^{70}	0.999
Peak d	158.08	177.74	−29340.06	−488.18	967.95	6.53×10^{101}	0.999
Peak e	169.16	187.18	−6652.43	−277.18	1152.09	2.28×10^{87}	0.999
Peak f	188.29	212.45	−12072.59	−200.88	549.34	6.48×10^{83}	0.999
Peak g	220.65	239.39	−17251.04	−718.79/−287.04	240.97	3.07×10^{18}	0.997
Total			−91155.69				

* Heat generation based on specific electrode.

parameters of these deconvoluted peaks were summarized and listed in Table 8. The heat generation per gram of each peak was also calculated by dividing the heat generation by the mass of the involved electrode.

The first two peaks should result from the decomposition of SEI and the melting of separator, respectively. By comparison with Fig. 9, it can be found the peak coupled with the electrolyte decomposition disappears, which is the result of decrease in the mass of electrolyte. With the gradual melting of separator, the area of contact at the interface of the positive and negative materials increases. Thermal behaviour of the resulting short circuit was shown as peak c. On account of the increase in the mass of the electrode materials, especially for Li$_x$CoO$_2$, peak c in Fig. 10 presents much larger heat generation and wider temperature range than peak e in Fig. 9.

Peak d compares well with peak b in Fig. 5 in the peak temperature and the heat generation. Accordingly, peak d is regarded as the disproportionation and decomposition of Li$_x$CoO$_2$. Peak e exhibits a parallel peak temperature to peak c in Fig. 7, but it presents larger heat generation and quite different thermal behaviour. Judging from the temperature range, peak e involves peak c and d in Fig. 7 arising from the intercalated lithium in Li$_x$C$_6$ and the electrolyte.

Peak f releases heat in the same way as peak c in Fig. 5, so it is can be explained as the result of the further decomposition of Li$_x$CoO$_2$. Nevertheless, by reason of the previous consumption of Li$_x$CoO$_2$, the heat generation of peak f is much smaller than that of peak c in Fig. 5. The temperature range of peak g coincides with the peak d in Fig. 5 and the peak f in Fig. 7. All the same, the heat generation of peak g is −718.79 J g^{-1} or −287.04 J g^{-1} based on the mass of negative or positive material, respectively. The two values are larger than the corresponding heat generation of peak d in Fig. 5 or peak f in Fig. 7, so peak g is believed to be composed of these two peaks.

From what has been discussed above, it can be seen that the decrease of electrolyte weakens the reactions associated with electrolyte, especially for the self-decomposition of the electrolyte under the elevated temperature. In the full cell system, the melting of separator activates the short circuit between the positive and negative electrode materials. The consequent heat generation and reactions decrease the thermal stability of the system. When the mass ratio of the full cell is same as that of the commercial full cell, the greatest contribution to the heat generation of the full cell system is the disproportionation and decomposition of Li$_x$CoO$_2$, and the second greatest contribution is arising from the short circuit.

4.5. Heating rate effect on the thermal behaviour of full cell

Fig. 11 shows the initial heat flow plot and the corresponding deconvoluted plots of full cell C at 0.5 °C min^{-1} heating rate. The
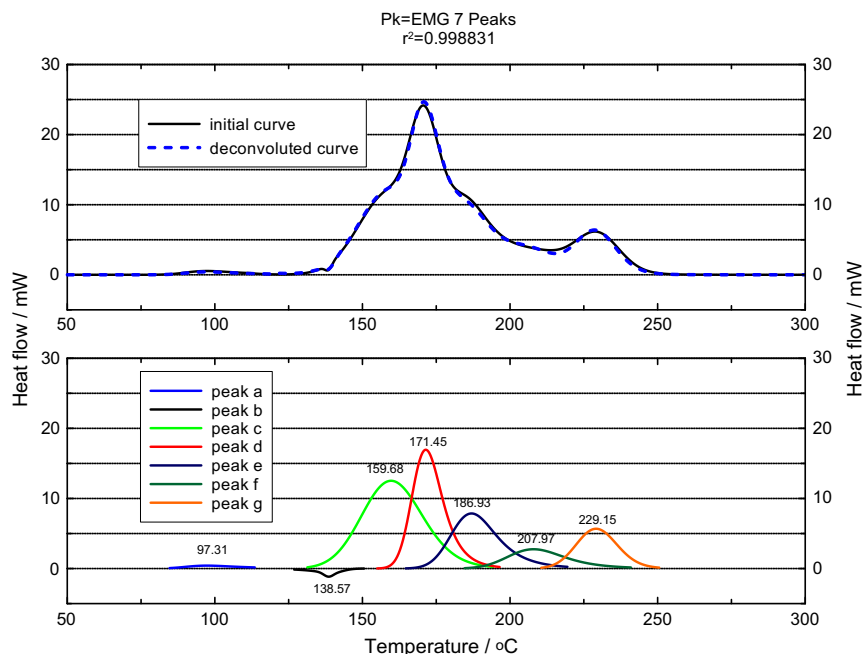
Fig. 11. Initial and deconvoluted C80 curves of heat flow versus temperature of full cell C at 0.5 °C min^{-1} heating rate.

Table 9
Thermodynamics and kinetics of full cell C at 0.5 °C min^{-1} heating rate.

	Onset temp. (°C)	Peak temp. (°C)	Reaction heat (mJ)	Reaction heat per gram* (J g^{-1})	Activation energy E (kJ mol^{-1})	Pre-exponential factor A (s^{-1})	Relativity R^2
Peak a	81.85	97.31	−1269.65	−48.83	116.11	4.19×10^{13}	0.994
Peak b	126.08	138.57	1083.77	252.04	–	–	–
Peak c	129.22	159. 68	−39337.68	–	281.76	1.13×10^{35}	0.998
Peak d	157.53	171.45	−27766.31	−455.19	973.87	2.97×10^{122}	0.999
Peak e	167.46	186.93	−19527.16	−751.04	1195.23	2.80×10^{89}	0.971
Peak f	184.95	207.97	−8411.55	−137.89	638.14	1.87×10^{203}	0.997
Peak g	213.31	229.15	−11895.92	−496.67/−195.02	259.66	4.23×10^{29}	0.989
Total			−108841.81				

* Heat generation based on specific electrode.

full cell C was composed of 61.3 mg Li$_x$CoO$_2$, 26.8 mg Li$_x$C$_6$, 24.5 mg 1.0 M LiPF$_6$/EC + DEC electrolyte, 5.2 mg separator, 11.2 mg aluminium foil and 18.0 mg copper foil. After deconvolution, seven exothermic peaks were picked from the plots, which were designated as peak a, b, c, d, e, f and g. Thermodynamic and kinetic parameters of these peaks were summarized and listed in Table 9. The heat generation per gram of each peak is calculated based on the mass of the related specific electrode in the following analysis.

Judging from the above study, the peaks a, b, c, d, e, f and g are ascribed to the SEI breakdown, melting of separator, positive–negative materials short circuit, Li$_x$CoO$_2$ disproportionation, lithium (in Li$_x$C$_6$)-electrolyte reaction, further decomposition of Li$_x$CoO$_2$ and oxidation of the thermal decomposition products of electrolyte/thermal reactions involving PVDF, respectively. When the heating rate increases from 0.2 °C min^{-1} to 0.5 °C min^{-1}, instantaneous heat flow of the system shows a significant increase. The case of peak c shows that its heat flow at the peak temperature increases from 3.13 mW to 12.58 mW. Nevertheless, since the heating time was shortened, the total heat generation of the system presents little change, which increases from −91155.69 to −108841.8 mJ. On the other hand, the temperature range of peaks a, b and c in Fig. 11 compares well with that of same peaks in Fig. 10. While peak d, e, f and g, which are after the short circuit peak (peak c), show lowered onset and peak temperatures. It can

be deduced that the heating rate plays an important role in accelerating the reaction in the full cell system after the occurrence of the short circuit.

5. Conclusions

A deconvolution-based peak separation method has been proposed for the study of the complicated thermal behaviours of Li-ion battery. By means of this method, process of thermal reactions occurring in the materials coexisting systems was explained. Thermal behaviours of electrolyte-single electrode system show that some electrolyte involved reactions were influenced by the decrease of the electrolyte content: heat generation of the oxidization of solvents and decompositon products of electrolyte decreases for the electrolyte-Li$_x$CoO$_2$ system; reactions between the intercalated lithium in Li$_x$C$_6$ and the electrolyte is dominated by the former; the new SEI layer decomposition disappears.

Based on the investigation of half-cell system, thermal reactions under elevated temperature for the Li$_x$CoO$_2$/Li$_x$C$_6$ full cell system was summed up as follows: SEI breakdown, melting of separator, short circuit of positive–negative materials, Li$_x$CoO$_2$ disproportionation, lithium (in Li$_x$C$_6$)-electrolyte reaction, further decomposition of Li$_x$CoO$_2$, oxidation of decomposition products of electrolyte and

thermal reactions involving PVDF, etc. The important thing to note is the short circuit between the positive and negative electrode materials activated by the melting of separator. The short circuit generates a large amount of heat and reduces the thermal stability of the system. Furthermore, full cells those like the commercial full cell start to release heat from 90 °C. The greatest contribution to the heat generation of these systems are the disproportionation and decomposition of Li_xCoO_2. Hence, enhancing the thermal stability of the SEI layer is the key factor to increase the onset temperature of the full cell; decreasing the heat generation of the positive material and improving the melting temperature is crucial to enhance the thermal stability of the full cell.

Acknowledgements

References

[1] Omar N, Monem MA, Firouz Y, Salminen J, Smekens J, Hegazy O, et al. Lithium iron phosphate based battery – assessment of the aging parameters and development of cycle life model. Appl Energ 2014;113:1575–85.

[2] Darcovich K, Henquin ER, Kenney B, Davidson IJ, Saldanha N, Beausoleil-Morrison I. Higher-capacity lithium ion battery chemistries for improved residential energy storage with micro-cogeneration. Appl Energ 2013;111:853–61.

[3] Waag W, Käbitz S, Sauer DU. Experimental investigation of the lithium-ion battery impedance characteristic at various conditions and aging states and its influence on the application. Appl Energ 2013;102:885–97.

[4] Barnett B, Ofer D, Sriramulu S, Stringfellow R. Lithium-ion batteries, safety. Batteries for sustainability. Springer; 2013. p. 285–318.

[5] Bandhauer TM, Garimella S, Fuller TF. A critical review of thermal issues in lithium-ion batteries. J Electrochem Soc 2011;158:R1–R25.

[6] Goodenough JB, Kim Y. Challenges for rechargeable Li batteries†. Chem Mater 2009;22:587–603.

[7] Jhu CY, Wang YW, Wen CY, Shu CM. Thermal runaway potential of LiCoO₂ and Li(Ni₁/₃Co₁/₃Mn₁/₃)O₂ batteries determined with adiabatic calorimetry methodology. Appl Energ 2012;100:127–31.

[8] Jin L, Lee P, Kong X, Fan Y, Chou S. Ultra-thin minichannel LCP for EV battery thermal management. Appl Energ 2014;113:1786–94.

[9] Lamb J, Orendorff CJ. Evaluation of mechanical abuse techniques in lithium ion batteries. J Power Sources 2014;247:189–96.

[10] Ren F, Cox T, Wang H. Thermal runaway risk evaluation of Li-ion cells using a pinch–torsion test. J Power Sources 2014;249:156–62.

[11] Wang Q, Ping P, Zhao X, Chu G, Sun J, Chen C. Thermal runaway caused fire and explosion of lithium ion battery. J Power Sources 2012;208:210–24.

[12] MacNeil D, Dahn J. The reaction of charged cathodes with nonaqueous solvents and electrolytes: I. Li₀.₅CoO₂. J Electrochem Soc 2001;148:A1205.

[13] Richard M, Dahn J. Accelerating rate calorimetry study on the thermal stability of lithium intercalated graphite in electrolyte. II. Modeling the results and predicting differential scanning calorimeter curves. J Electrochem Soc 1999;146:2078.

[14] Jhu C-Y, Wang Y-W, Shu C-M, Chang J-C, Wu H-C. Thermal explosion hazards on 18650 lithium ion batteries with a VSP2 adiabatic calorimeter. J Hazard Mater 2011;192:99–107.

[15] Holzapfel M, Alloin F, Yazami R. Calorimetric investigation of the reactivity of the passivation film on lithiated graphite at elevated temperatures. Electrochim Acta 2004;49:581–9.

[16] Wen C-Y, Jhu C-Y, Wang Y-W, Chiang C-C, Shu C-M. Thermal runaway features of 18650 lithium-ion batteries for LiFePO₄ cathode material by DSC and VSP2. J Therm Anal Calorim 2012;109:1297–302.

[17] Ping P, Wang Q, Sun J, Xiang H, Chen C. Thermal stabilities of some lithium salts and their electrolyte solutions with and without contact to a LiFePO₄ electrode. J Electrochem Soc 2010;157. A1170-A6.

[18] Wang Q, Ping P, Sun J, Chen C. The effect of mass ratio of electrolyte and electrodes on the thermal stabilities of electrodes used in lithium ion battery. Thermochim Acta 2011;517:16–23.

[19] Saito Y. Thermal behaviors of lithium-ion batteries during high-rate pulse cycling. J Power Sources 2005;146:770–4.

[20] Al Hallaj S, Prakash J, Selman J. Characterization of commercial Li-ion batteries using electrochemical–calorimetric measurements. J Power Sources 2000;87:86–94.

[21] Feng X, Fang M, He X, Ouyang M, Lu L, Wang H, et al. Thermal runaway features of large format prismatic lithium ion battery using extended volume accelerating rate calorimetry. J Power Sources 2014.

[22] Dagan S. Comparison of gas chromatography-pulsed flame photometric detection-mass spectrometry, automated mass spectral deconvolution and identification system and gas chromatography–tandem mass spectrometry as tools for trace level detection and identification. J Chromatogr A 2000;868:229–47.

[23] Hatchard T, MacNeil D, Basu A, Dahn J. Thermal model of cylindrical and prismatic lithium-ion cells. J Electrochem Soc 2001;148. A755-A61.

[24] Kim G-H, Pesaran A, Spotnitz R. A three-dimensional thermal abuse model for lithium-ion cells. J Power Sources 2007;170:476–89.

[25] Elsabee M, Prankerd R. Solid-state properties of drugs. II. Peak shape analysis and deconvolution of overlapping endotherms in differential scanning calorimetry of chiral mixtures. Int J Pharm 1992;86:211–9.

[26] Yau W. Characterizing skewed chromatographic band broadening. Anal Chem 1977;49:395–8.

[27] Foley JP, Dorsey JG. Equations for calculation of chromatographic figures of merit for ideal and skewed peaks. Anal Chem 1983;55:730–7.

[28] Jönsson JÅ. Chromatographic theory and basic principles. CRC Press; 1987.

[29] Ping P, Wang Q, Sun J, Feng X, Chen C. Effect of sulfites on the performance of LiBOB/γ-butyrolactone electrolytes. J Power Sources 2011;196:776–83.

[30] Koltypin M, Aurbach D, Nazar L, Ellis B. On the stability of LiFePO₄ olivine cathodes under various conditions (electrolyte solutions, temperatures). Electrochem Solid-State Lett 2007;10. A40-A4.

[31] Sloop SE, Kerr JB, Kinoshita K. The role of Li-ion battery electrolyte reactivity in performance decline and self-discharge. J Power Sources 2003;119:330–7.

[32] Gnanaraj J, Zinigrad E, Asraf L, Gottlieb H, Sprecher M, Aurbach D, et al. The use of accelerating rate calorimetry (ARC) for the study of the thermal reactions of Li-ion battery electrolyte solutions. J Power Sources 2003;119:794–8.

[33] Gnanaraj J, Zinigrad E, Asraf L, Gottlieb H, Sprecher M, Schmidt M, et al. A detailed investigation of the thermal reactions of LiPF₆ solution in organic carbonates using ARC and DSC. J Electrochem Soc 2003;150. A1533-A7.

[34] Spotnitz R, Franklin J. Abuse behavior of high-power, lithium-ion cells. J Power Sources 2003;113:81–100.

[35] Zhao LW, Watanabe I, Doi T, Okada S, Yamaki J. TG–MS analysis of solid electrolyte interphase (SEI) on graphite negative-electrode in lithium-ion batteries. J Power Sources 2006;161:1275–80.

[36] Watanabe I, Yamaki J. Thermalgravimetry-mass spectrometry studies on the thermal stability of graphite anodes with electrolyte in lithium-ion battery. J Power Sources 2006;153:402–4.

[37] Wang QS, Sun JH, Yao XL, Chen CH. Thermal behavior of lithiated graphite with electrolyte in lithium-ion batteries. J Electrochem Soc 2006;153. A329-A33.

[38] Yamaki J, Takatsuji H, Kawamura T, Egashira M. Thermal stability of graphite anode with electrolyte in lithium-ion cells. Solid State Ion 2002;148:241–5.

[39] Andersson AM, Edstrom K, Rao N, Wendsjo A. Temperature dependence of the passivation layer on graphite. J Power Sources 1999;82:286–90.

[40] Wang Q, Sun J, Yao X, Chen C. Thermal behavior of lithiated graphite with electrolyte in lithium-ion batteries. J Electrochem Soc 2006;153:A329–33.

[41] Gray FM. Solid polymer electrolytes: VCH New Tork etc.; 1991.